Geometrical incompatibility guides pattern selection in growing bilayer tubes

Congshan Liu[a], Yangkun Du[c], Kecheng Li[a], Yinnan Zhang[a], Zilong Han[d,e], Yangyang Zhang[b,*], Shaoxing Qu[d,e], Chaofeng Lü[b,a,e,f,*]

[a]*Department of Civil Engineering, Zhejiang University, Hangzhou 310058, P.R. China;*

[b]*Faculty of Mechanical Engineering and Mechanics, Ningbo University, Ningbo 315211, P.R. China;*

[c]*School of Mathematics and Statistics, University of Glasgow, Glasgow G12 8QQ, UK.*

[d]*State Key Laboratory of Fluid Power and Mechatronic System, Center for X-Mechanics, Department of Engineering Mechanics, Zhejiang University, 38 Zheda Road, Hangzhou 310027, China;*

[e]*Key Lab of Soft Machines and Smart Devices of Zhejiang Province, Zhejiang University, Hangzhou 310027, P.R. China;*

[f]*Soft Matter Research Center, Zhejiang University, Hangzhou 310027, P. R. China;*

Abstract

Pattern selection and subsequent morphological evolution are of remarkable significance, since they are critical for living creatures to fulfill certain biological functions and also have widespread potential applications from disease diagnosis to advanced manufacturing. Geometrical incompatibility is omnipresent in biological systems and plays a critical role in pattern selection of the growing soft biological tissues. However, how geometrical incompatibility guides pattern selection in growing soft matter remains poorly understood. Here, we present a theoretical model to investigate the influence of geometrical incompatibility on pattern selection of growing bilayer tubes. Our linear stability analysis illustrates that an increase of the geometrical incompatibility parameter provokes the instability pattern transition from a longitudinal pattern to a two-dimensional (2D) pattern and then to a circumferential pattern. Based on the theoretical model, a series of quantificational experiments and finite element simulations are implemented to study how geometrical incompatibility guides pattern selection of growing bilayer tubes and explore the post-buckling evolution of the emerging patterns. Both the numerical simulations and experimental observations agree well with our theoretical predictions. In particular, with further growth far beyond the threshold, a secondary bifurcation is observed in the post-buckling evolution of the 2D pattern. This study suggests that geometrical incompatibility can serve as an implementable experimental tool to quantificationally guide pattern selection and subsequent morphological evolution of growing soft matter, which can be used for growth self-assembly and multifunctional surface manufacturing.

Keywords: Geometrical incompatibility; Swelling experiment; Bilayer tube; Pattern formation; Post-buckling

*Corresponding authors

[1]lucf@zju.edu.cn, (Chaofeng Lü)

[2]zhangyangyang@nbu.edu.cn, (Yangyang Zhang)

1. Introduction

Diverse surface patterns across length scales in soft matter are ubiquitous in nature. Numerous instances can be found in our surroundings, including various shapes of plant leaves (Huang et al., 2018; Dervaux and Ben Amar, 2008; Xu et al., 2020a), wrinkling and cusp formation of spherical fruits and vegetables (Yin et al., 2009; Liu et al., 2020; Chakrabarti et al., 2021), buckling instability of growing tumors (Ben Amar et al., 2011; Ciarletta, 2013), morphological evolution of the gut during embryogenesis (Savin et al., 2011; Shyer et al., 2013), and pattern formation in dehydrated leaves, green pea and many types of fruits (Xiao and Chen, 2011; Li et al., 2011b; Liu et al., 2015). These specific morphologies in living creatures are indispensable to fulfill certain biological functions. Meanwhile, morphological instabilities have attracted considerable attentions due to their widespread potential applications from the diagnosis of certain diseases (Li et al., 2011a; Ben Amar and Jia, 2013), deterministic organoid patterning (Gjorevski et al., 2022), biomimetic 4D printing (Sydney Gladman et al., 2016; Ge et al., 2013; Du et al., 2020), multifunctional surface designs (Barros et al., 2012; Bae et al., 2017; Cheewaruangroj and Biggins, 2019; Xu et al., 2020b), to the fabrication of stimuli-responsive hydrogel composites (Erb et al., 2013; Thérien-Aubin et al., 2013). Therefore, understanding the underlying mechanism of pattern selection and morphological evolution of growable soft matter is of remarkable significance.

Abundant surface patterns in biological systems are generally induced by differential growth or shrinkage. Much effort has been devoted to studying the mechanical mechanism underlying the morphogenesis induced by volumetric growth (Rodriguez et al., 1994; Ben Amar and Goriely, 2005; Goriely and Ben Amar, 2005; Goriely, 2017). The basic theoretical framework of tissue growth has been established, and it was demonstrated that both differential growth and anisotropic growth play a crucial role in the mechanical response and morphological instability of soft tissues. Subsequently, the volumetric growth theory was widely employed to experimentally and theoretically investigate the circumferential instabilities of hydrogel ring and tubular soft tissue (Dervaux and Ben Amar, 2011; Dervaux et al., 2011; Li et al., 2011a; Moulton and Goriely, 2011). In practice, the instability pattern in tubular soft tissue can be circumferential, longitudinal and even 2D (Wilcox et al., 2012). Then, Ciarletta and his collaborators (Ciarletta et al., 2014; Balbi et al., 2015) proposed a three-dimensional model to investigate surface pattern formation and performed a series of finite element (FE) simulations to explore the post-buckling evolution of a growing bilayer tubular tissue with axial constraint. Nevertheless, these models were limited to the assumption that biological tissue is initially stress-free, which is inconsistent with the experimental observations that a biological tissue is residually stressed at almost any growth state (Stylianopoulos et al., 2012).

In order to characterize the initial stressed elastic solids, Shams et al. (2011) proposed a free energy density that depends on the elastic strains and initial residual stresses. Besides, Gower et al. (2015) presented the initial stress symmetry (ISS) condition to restrict the possible choices of free energy densities. Using the new constitutive model, Ciarletta et al. (2016) studied the morphological instability of residually stressed tubular soft tissue. To describe the growth and wrinkling of initially stressed biological tissue, a modified multiplicative decomposition model that can concatenate any two growth states of an initially stressed soft tissue was established by Du et al. (2018). Soon after, Du and his collaborators developed a three-dimensional model and implemented a qualitative control experiment to investigate the influence of initial residual stress on the growth and pattern formation of bilayer tubular tissue (Du et al., 2019a,b). However, quantificational experiments for investigating pattern selection of residually stressed growing soft matter have not been carried out up to now, since the complex distribution of the residual stresses is difficult to accurately reproduce in the experiments. Therefore, it is of great significance to

propose a quantificationally implementable strategy to experimentally investigate pattern selection in residually stressed growing soft matter.

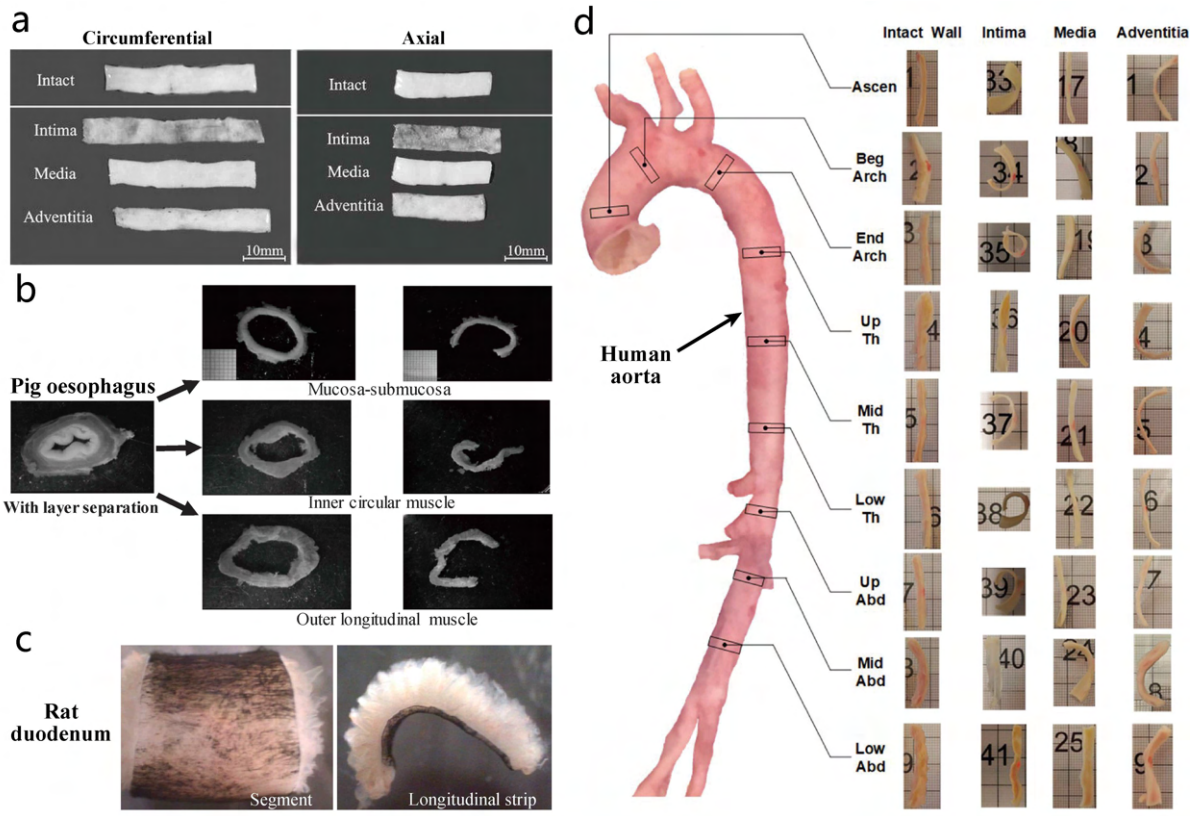

Figure 1: Evidence of geometrical incompatibility in soft biological tissues. (a) Anatomical separation of fresh human aorta shows that the layer-specific geometrical incompatibilities reside in both circumferential and axial directions (Holzapfel et al., 2007); (b) Illustration of the existence of geometrical incompatibility by microsurgical separation of pig oesophagus into three layers in the no-load state (left) and zero-stress state (right) (Zhao et al., 2007); (c) Rat duodenum strips bent outwards in the longitudinal direction after longitudinal cutting (Dou et al., 2006); (d) The intact wall and separated layer strips have different opening angles in their zero-stress state, after removal from the nine consecutive aortic levels in circumferential directions (Sokolis et al., 2021).

Geometrical incompatibility is ubiquitous in living creatures (Buganza Tepole et al., 2016; Rebocho et al., 2015), especially in layered biological tissues (Fig.1), and has been identified as the origin of residual stresses in biological tissues (Sommer et al., 2010; Steinmann, 2015). Owing to easy accessibility with high precision, geometrical incompatibility has been adopted to shape numerous elegant patterns in soft matter without growth (Aharoni et al., 2017; Caruso et al., 2018; Davidovitch et al., 2019). Here, we propose using geometrical incompatibility to quantificationally guide pattern selection in growing soft matter, both theoretically and experimentally, and explore the post-buckling evolution of the emerging patterns.

In this paper, we attempt to theoretically and experimentally explore the effect of geometrical incompatibility on pattern selection in growing soft matter. Based on the modified multiplicative decomposition model, we establish an improved theoretical model to investigate how geometrical incompatibility governs the onset of instability and pattern selection of a growing bilayer tube by quantificationally prescribing a residual stress field. Accordingly, a series of quantificational experiments are implemented to investigate patterns formation and subsequent morphological evolutions of the growing bilayer tubes. Morphological phase diagrams for patterns selection, obtained from

the linear stability analyses and verified both numerically and experimentally, illustrate how geometrical incompatibility guides pattern selection of the growing bilayer tubes.

This paper is organized as follows. Section 2 gives an initial geometrically incompatible bilayer tube, and then theoretically analyzes the distributions of residual stresses induced by geometrical incompatibility and differential growth. In Section 3, we perform a linear stability analysis based on the incremental theory to derive the critical instability condition and corresponding wavenumbers. Section 4 implements a wide class of swelling experiments and a series of FE simulations to validate the results of our theoretical analysis, as well as explore the morphological evolutions of the emerging patterns. The results are provided in Section 5, including the phase diagrams on patterns selection and the post-buckling evolution of the instability patterns. Finally, the main conclusions are summarized in Section 6.

2. Growth of geometrically incompatible bilayer cylindrical tubes

2.1. Residual stresses induced by geometrical incompatibility

Consider a geometrically incompatible bilayer cylindrical tube constructed from two hyperelastic and isotropic tubes with the same length. Here, we introduce the dimensionless parameter δ to denote the degree of geometrical incompatibility of the bilayer cylindrical tube. We begin from the stress-free but geometrically incompatible state in which the outer tube has an inner radius B and an outer radius C, while the inner tube has an inner radius A and an outer radius $B(1+\delta)$, as shown in Fig.2. In the following, the physical fields of the out tube and inner tube are indicated by the superscripts o and i, respectively. Accordingly, the initial thicknesses of the outer tube and the inner tube are $H^o = C - B$ and $H^i = B(1+\delta) - A$, respectively.

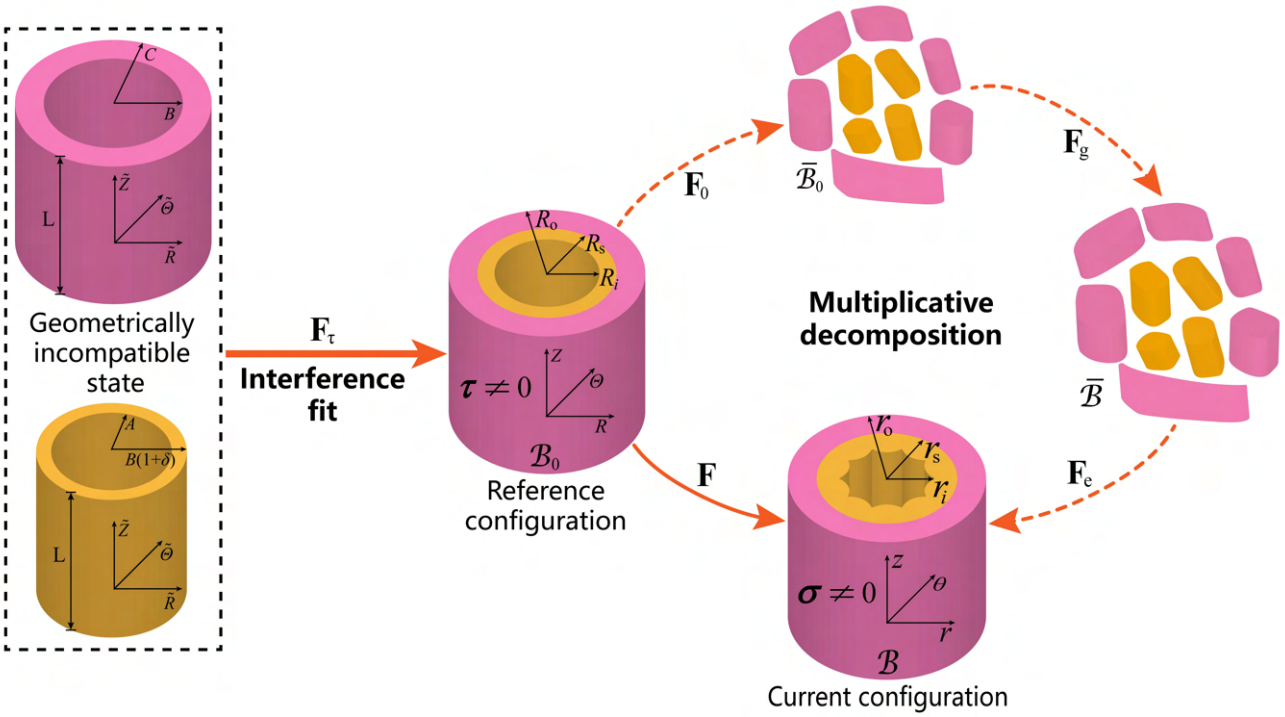

Figure 2: Kinematics of a bilayer tube from the geometrically incompatible state to the residually stressed reference configuration $\mathcal{B}_0$ and then to the grown current configuration $\mathcal{B}$.

Here, we designate the cylindrical coordinates $\tilde{\mathbf{X}} = \left(\tilde{R}, \tilde{\Theta}, \tilde{Z}\right)$, $\mathbf{X} = (R, \Theta, Z)$ and $\mathbf{x} = (r, \theta, z)$ for the geometrically incompatible state, the reference configuration $\mathcal{B}_0$ and the current configuration $\mathcal{B}$, respectively. Fig.2 depicts the interference fit assembly and growth process of the geometrically incompatible bilayer tube. The inner tube is radially stretched or compressed to perfectly fit inside the outer tube. The area along the interface between the two tubes is glued to achieve perfect adhesion, and the bilayer tube is allowed to relax. We denote the inner, interface, and outer radii in the reference configuration $\mathcal{B}_0$ as R_i, R_s and R_o, respectively. After growth, the internal, contact, and external radii in the current configuration $\mathcal{B}$ become r_i, r_s and r_o, respectively.

Due to geometrical incompatibility between two layers, the interference fit assembly will generate inhomogeneous deformation and residual stress in the bilayer tube. We adopt the incompressible neo-Hookean constitutive model to characterize the deformations of both layers, with elastic energy densities

$$W^k = \frac{\mu^k}{2}\left[\left(\lambda_R^k\right)^2 + \left(\lambda_\Theta^k\right)^2 + \left(\lambda_Z^k\right)^2 - 3\right], \tag{1}$$

where μ^k are the shear modulus with $k = \{i, o\}$, $\lambda_R^k, \lambda_\Theta^k, \lambda_Z^k$ are the radial, circumferential, and axial stretches, respectively. For the sake of notation simplicity, from now on, we will omit the superscript k unless explicitly stated.

The interference fit assembly of the bilayer cylindrical tube is assumed as an axisymmetric plane strain model, and then the deformation gradient tensor can be given by

$$\mathbf{F}_\tau = \mathrm{diag}\left(\frac{\mathrm{d}R}{\mathrm{d}\tilde{R}},\ \frac{R}{\tilde{R}},\ 1\right), \tag{2}$$

with $\det \mathbf{F}_\tau = 1$ imposed by the incompressibility. Then, using the constitutive law in Eq.(1), the principal initial residual stresses in the bilayer cylindrical tube are obtained as

$$\begin{aligned} \tau_{RR} &= \mu\lambda^{-2} - p_\tau, \\ \tau_{\Theta\Theta} &= \mu\lambda^{2} - p_\tau, \\ \tau_{ZZ} &= \mu - p_\tau, \end{aligned} \tag{3}$$

where $\lambda = R/\tilde{R}$ and p_τ is the hydrostatic pressure to be determined. In the absence of the body force, the initial stresses should satisfy the following equation of equilibrium,

$$\frac{\partial \tau_{RR}}{\partial R} + \frac{\tau_{RR} - \tau_{\Theta\Theta}}{R} = 0. \tag{4}$$

Using the stress-free boundary condition at the inner and outer surfaces, we have

$$\tau_{RR}^i\big|_{R=R_i} = 0, \qquad \tau_{RR}^o|_{R=R_o} = 0. \tag{5}$$

Besides, since the interface between the two layers is perfect, the radial stresses at the interface are required to be continuous, being

$$\tau_{RR}^i\big|_{R=R_s} = \tau_{RR}^o|_{R=R_s}. \tag{6}$$

Using Eq.(3) and replacing the variable R by λ, Eq.(4) can be rewritten as

$$\frac{\partial \tau_{RR}}{\partial \lambda} = -\mu\left(\lambda^{-1} + \lambda^{-3}\right). \tag{7}$$

Integrating Eq.(7) with the boundary conditions in Eq.(5), the radial stresses of both layers are derived as

$$\tau^i_{RR} = \frac{\mu^i}{2}\left(\frac{\tilde{R}^2}{R_i^2+\tilde{R}^2-A^2}-\frac{A^2}{R_i^2}\right)+\mu^i\ln\left(\frac{\tilde{R}R_i}{A\sqrt{R_i^2+\tilde{R}^2-A^2}}\right),$$
$$\tau^o_{RR} = \frac{\mu^o}{2}\left(\frac{\tilde{R}^2}{R_o^2+\tilde{R}^2-C^2}-\frac{C^2}{R_o^2}\right)+\mu^o\ln\left(\frac{\tilde{R}R_o}{C\sqrt{R_o^2+\tilde{R}^2-C^2}}\right), \tag{8}$$

where $R_i=\sqrt{R_s^2+A^2-B^2(1+\delta)^2}$, and $R_o=\sqrt{R_s^2+C^2-B^2}$ with R_s to be determined. Substituting Eq.(8) into Eq.(6), the continuity condition can be reduced to the dimensionless form:

$$\frac{1}{2}\left(\frac{\bar{B}^2(1+\delta)^2}{\bar{R}_s{}^2}-\frac{[\bar{B}(1+\delta)-(H^i/H^o)(1-\bar{B})]^2}{\bar{R}_i{}^2}\right)-\frac{\mu^o}{\mu^i}\ln\left(\frac{\bar{B}\sqrt{\bar{R}_s{}^2+1-\bar{B}^2}}{\bar{R}_s}\right)$$
$$+\ln\left(\frac{\bar{B}\bar{R}_i(1+\delta)}{\bar{R}_s[\bar{B}(1+\delta)-(H^i/H^o)(1-\bar{B})]}\right)-\frac{\mu^o}{2\mu^i}\left(\frac{\bar{B}^2}{\bar{R}_s{}^2}-\frac{1}{\bar{R}_s{}^2+1-\bar{B}^2}\right)=0. \tag{9}$$

Where $\bar{R}_i=\sqrt{\bar{R}_s{}^2-\bar{B}^2(1+\delta)^2+[\bar{B}(1+\delta)-(H^i/H^o)(1-\bar{B})]^2}$ with $\bar{R}_s=R_s/C$, and $\bar{B}=B/C$. The unknown interface radii R_s can be determined by numerically solving Eq.(9) with an explicit Newton method. Finally, the principal residual stresses induced by geometrical incompatibility can be calculated.

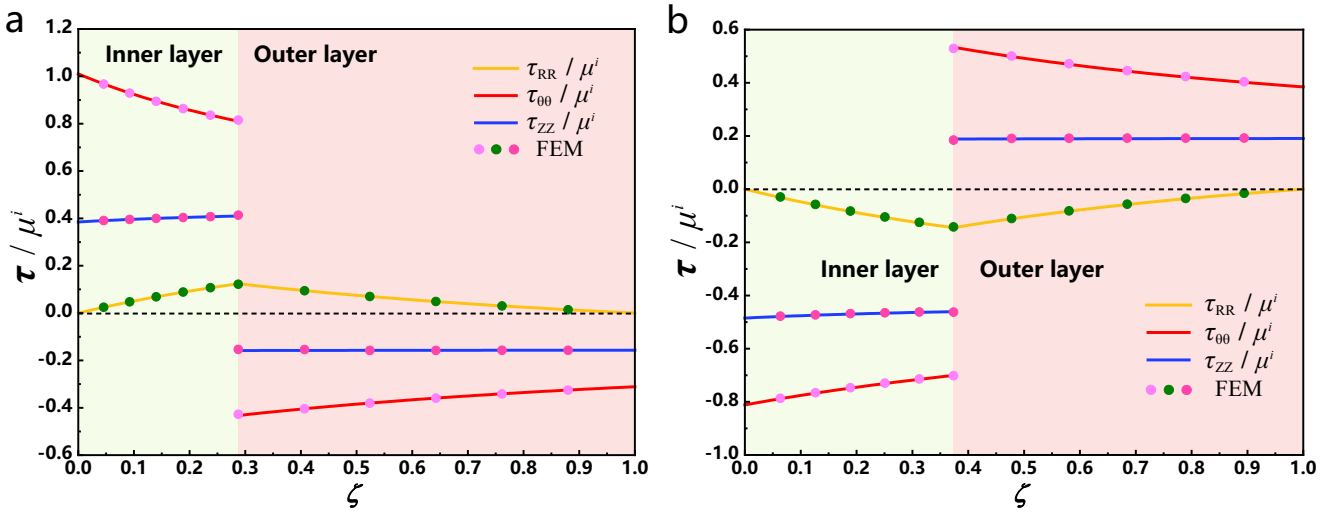

Figure 3: Transmural distributions of the normalized residual stresses induced by the geometrical incompatibility of the bilayer tubes that $\delta=-1/6$ (a), $\delta=1/6$ (b), fixing $B/C=0.75$, $\mu^o/\mu^i=10$, $H^i/H^o=0.5$.

Fig.3 depicts the dimensionless transmural distributions of the residual stresses induced by geometrical incompatibility in the cylindrical bilayer tube with $\zeta=(R-R_i)/(R^o-R_i)$. Here, we are interested in the distribution of residual stresses in the inner layer. It is apparent that a negative geometrical incompatibility parameter ($\delta<0$) can induce radial tensile stress, as well as circumferential and axial compressive stresses. By contrast, a positive geometrical incompatibility

parameter ($\delta > 0$) generates radial compressive stress, circumferential and axial tensile stresses in the inner layer. The maximum circumferential and axial stresses arise at the inner surface of the bilayer tube. In particular, our theoretical solution show an excellent agreement with the results of FE simulation.

2.2. Growth of residually stressed bilayer tubes

According to the modified multiplicative decomposition growth model (Du et al., 2018), the overall deformation gradient tensor $\mathbf{F} = \partial\mathbf{x}/\partial\mathbf{X}$ can be decomposed multiplicatively as

$$\mathbf{F} = \mathbf{F}_e\mathbf{F}_g\mathbf{F}_0, \tag{10}$$

in which $\mathbf{F}_e$, $\mathbf{F}_g$ and $\mathbf{F}_0$ stand for the elastic deformation tensor, the pure growth tensor, and the initial elastic deformation tensor, respectively. The initial elastic deformation tensor $\mathbf{F}_0$ is induced by releasing the initial residual stress, and is quantitively the same as $\mathbf{F}_\tau^{-1}$ here. To be consistent with the following swelling experiment, we assume that both layers grow isotropically as $\mathbf{F}_g^k = \mathrm{diag}\{g^k,\ g^k,\ g^k\}$ with $k = \{i, o\}$, where g^i and g^o are the growth factors of the inner layer and outer layer, respectively. For the sake of simplicity, we defined $\bar{g} = g^i/g^o$ as the differential growth ratio of the bilayer cylindrical tube. Then, using the expression of the initial residual stress $\boldsymbol{\tau} = \mu\mathbf{F_0}^{-1}\mathbf{F_0}^{-T} - p_0\mathbf{I}$, the constitutive equation can be derived as

$$\boldsymbol{\sigma} = J_g^{-\frac{2}{3}}\left(\mathbf{F}\boldsymbol{\tau}\mathbf{F}^T + p_0\mathbf{F}\mathbf{F}^T\right) - p\mathbf{I}, \tag{11}$$

where $J_g = \det\mathbf{F}_g$ indicates the volume change ratio and $p_0,\ p$ are the Lagrange multipliers in the reference and current configurations, respectively.

Here, we characterize the geometrical deformation of the growing residually stressed bilayer cylindrical tube by prescribing $\mathbf{F} = \mathrm{diag}\,(dr/dR,\ r/R,\ 1)$. The axial and tangential displacements at the two ends of the bilayer tube are fully constrained. With the traction free boundary conditions $\sigma_{rr}^i|_{r=r_i} = 0$, $\sigma_{rr}^o|_{r=r_o} = 0$, the continuity at the contact interface $\sigma_{rr}^i|_{r=r_s} = \sigma_{rr}^o|_{r=r_s}$, as well as the incompressibility condition $\det\left(\mathbf{F}\mathbf{F}_g^{-1}\right) = 1$, the radial Cauchy stresses of both layers are obtained as

$$\begin{aligned}
\sigma_{rr}^i &= \int_0^{\xi^i}\left[\left(\tau_{\Theta\Theta}^i + p_0^i\right)\left(\frac{r^i}{R^i}\right)^2 - \left(\tau_{RR}^i + p_0^i\right)\left(\frac{J_g^i R^i}{r^i}\right)^2\right]\times\frac{\left(J_g^i\right)^{\frac{1}{3}}H_\tau^i\left(\xi^i H_\tau^i + R_i\right)}{J_g^i\xi^i H_\tau^i\left(\xi^i H_\tau^i + 2R_i\right) + r_i^2}\,\mathrm{d}\xi^i,\\
\sigma_{rr}^o &= \int_1^{\xi^o}\left[\left(\tau_{\Theta\Theta}^o + p_0^o\right)\left(\frac{r^o}{R^o}\right)^2 - \left(\tau_{RR}^o + p_0^o\right)\left(\frac{J_g^o R^o}{r^o}\right)^2\right]\times\frac{\left(J_g^o\right)^{\frac{1}{3}}H_\tau^o\left(\xi^o H_\tau^o - R_o\right)}{J_g^o\xi^o H_\tau^o\left(\xi^o H_\tau^o - 2R_o\right) + r_o^2}\,\mathrm{d}\xi^o,
\end{aligned} \tag{12}$$

where $H_\tau^i = R_s - R_i,\ \xi^i = (R - R_i)/H_\tau^i,\ \ H_\tau^o = R_o - R_s,\ \xi^o = (R_o - R)/H_\tau^o$. Finally, we are able to calculate the radial, circumferential and axial components of the Cauchy stress in the current configuration.

Fig.4 shows the effect of geometrical incompatibility on the circumferential compressive stresses $\sigma_{\theta\theta}$ and longitudinal compressive stresses σ_{zz} at the inner surface, during the differential growth. It reveals that both circumferential and axial compressive stresses are generated and accumulated as the differential growth ratio $\bar{g}$ increases. During the differential growth, a positive geometrically incompatible ($\delta = 1/6$) bilayer tube generally generates a higher level of compressive stresses than the initial geometrically compatible ($\delta = 0$) counterpart, both circumferentially and axially. By contrast, the negative geometrically incompatible ($\delta = -1/6$) bilayer tube generates initial tensile

stresses, which transform into compressive stresses with gradual growth, and the compressive stresses are smaller than that in the initial geometrically compatible counterpart with the same differential growth ratio. The compressive stress, either circumferential or axial, tends to trigger the instability of the inner layer when it accumulates to a critical value.

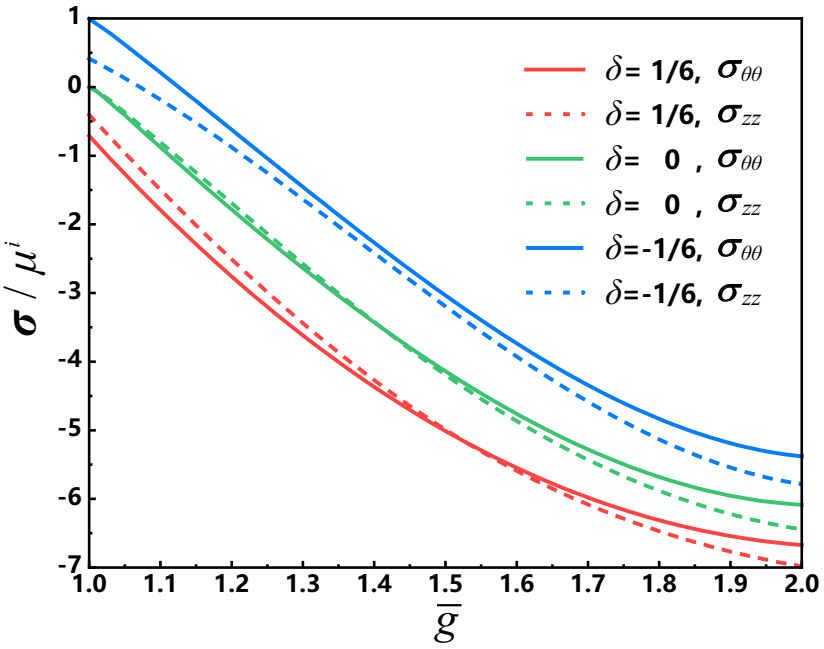

Figure 4: Normalized circumferential and longitudinal stresses at the inner surface of initial geometrically incompatible bilayer cylindrical tubes against the differential growth ratio $\bar{g}$. The curves are shown for constant $B/C = 0.75$, $\mu^o/\mu^i = 7.5$, and $H^i/H^o = 0.5$ at varying $\delta = \{1/6,\ 0,\ -1/6\}$.

3. Linear stability analysis

3.1. Theoretical formulations

In order to study the critical instability and pattern selection of the initial geometrically incompatible bilayer tube induced by differential growth, we perform a linear stability analysis based on the incremental theory for tissue growth (Ben Amar and Goriely, 2005). Then the incremental displacement field can be expressed as

$$\dot{\boldsymbol{x}} = u(r,\theta,z)\boldsymbol{e}_r + v(r,\theta,z)\boldsymbol{e}_\theta + w(r,\theta,z)\boldsymbol{e}_z, \tag{13}$$

where the functions u, v, w are incremental displacements, and $\boldsymbol{e}_r$, $\boldsymbol{e}_\theta$, $\boldsymbol{e}_z$ represent the unit base vectors of the cylindrical coordinate system. Hence, the incremental displacement gradient tensor $\dot{\boldsymbol{F}}_{\mathrm{I}}$ becomes

$$\dot{\boldsymbol{F}}_{\mathrm{I}} = \frac{\partial \dot{\boldsymbol{x}}}{\partial \boldsymbol{x}} = \begin{bmatrix} \frac{\partial u}{\partial r} & \frac{1}{r}\left(\frac{\partial u}{\partial \theta} - v\right) & \frac{\partial u}{\partial z} \\ \frac{\partial v}{\partial r} & \frac{1}{r}\left(\frac{\partial v}{\partial \theta} + u\right) & \frac{\partial v}{\partial z} \\ \frac{\partial w}{\partial r} & \frac{1}{r}\frac{\partial w}{\partial \theta} & \frac{\partial w}{\partial z} \end{bmatrix}, \tag{14}$$

together with the incremental incompressibility condition:

$$\operatorname{tr} \dot{\boldsymbol{F}}_{\mathrm{I}} = \frac{\partial u}{\partial r} + \frac{1}{r}\left(\frac{\partial v}{\partial \theta} + u\right) + \frac{\partial w}{\partial z} = 0. \tag{15}$$

Then, the incremental nominal stress $\dot{\boldsymbol{S}}$ in push-forward form can be obtained as

$$\dot{\boldsymbol{S}}_{\mathrm{I}ij} = \mathcal{A}^{\mathrm{I}}_{\mathrm{e}ijkl}\dot{F}_{\mathrm{I}lk} - \dot{p}\delta_{ij} + p\dot{F}_{\mathrm{I}ij}, \tag{16}$$

where $\dot{p}$ is the incremental Lagrange multiplier and $\mathcal{A}^{\mathrm{I}}_{\mathrm{e}ijkl} = F_{\mathrm{e}i\alpha}F_{\mathrm{e}k\beta}\frac{\partial^2 W}{\partial F_{\mathrm{e}j\alpha}\partial F_{\mathrm{e}l\beta}}$ are the instantaneous elastic moduli. In the absence of body forces, we can postulate the incremental equilibrium equation and boundary condition as follows:

$$\mathrm{div}\dot{\mathbf{S}}_{\mathrm{I}} = 0, \qquad \dot{\mathbf{S}}^T_{\mathrm{I}}\mathbf{n} = 0. \tag{17}$$

To determine the critical condition of surface instability, we consider the variable separation of incremental fields in the following form:

$$\begin{aligned}
u &= U(r)\cos(m\theta)\cos(k_z z), & \dot{S}_{Irr} &= \Sigma_{rr}(r)\cos(m\theta)\cos(k_z z),\\
v &= V(r)\sin(m\theta)\cos(k_z z), & \dot{S}_{Ir\theta} &= \Sigma_{r\theta}(r)\sin(m\theta)\cos(k_z z),\\
w &= W(r)\cos(m\theta)\sin(k_z z), & \dot{S}_{Irz} &= \Sigma_{rz}(r)\cos(m\theta)\sin(k_z z),\\
\dot{p} &= P(r)\cos(m\theta)\cos(k_z z), &&
\end{aligned} \tag{18}$$

where m and $k_z = 2n\pi/L$ (with $m, n \in \mathbb{N}$) are the circumferential and axial modes respectively, and the amplitudes U, V, W, P, Σ_{rr}, $\Sigma_{r\theta}$, Σ_{rz} are scalar functions of r only. Thereafter, the governing equations in Eqs.(15) and (17) can be rewritten in the *Stroh form*:

$$\frac{\mathrm{d}}{\mathrm{d}r}\boldsymbol{\eta}(r) = \frac{1}{r}\boldsymbol{G}(r)\boldsymbol{\eta}(r), \tag{19}$$

where $\boldsymbol{\eta} = [\mathbf{U}, r\mathbf{S}]^T$ is the displacement-traction vector, in which $\mathbf{U} = [U, V, W]^T$ and $\mathbf{S} = [\Sigma_{rr}, \Sigma_{r\theta}, \Sigma_{rz}]^T$. Here, $\boldsymbol{G}$ is the so-called *Stroh matrix* that can be decomposed into the following block form:

$$\mathbf{G} = \begin{pmatrix} \mathbf{G}_1 & \mathbf{G}_2 \\ \mathbf{G}_3 & -\mathbf{G}_1^T \end{pmatrix}. \tag{20}$$

The components of the 3×3 sub-blocks are given by

$$\mathbf{G}_1 = \begin{pmatrix} -1 & -m & -k_z r \\ \frac{mp}{\mathcal{A}^I_{\mathrm{e}r\theta r}} & \frac{p}{\mathcal{A}^I_{\mathrm{e}r\theta\theta}} & 0 \\ \frac{k_z r p}{\mathcal{A}^I_{\mathrm{e}rzrz}} & 0 & 0 \end{pmatrix}, \mathbf{G}_2 = \begin{pmatrix} 0 & 0 & 0 \\ 0 & \frac{1}{\mathcal{A}^I_{\mathrm{e}r\theta r\theta}} & 0 \\ 0 & 0 & \frac{1}{\mathcal{A}^I_{\mathrm{e}rzrz}} \end{pmatrix}, \mathbf{G}_3 = \begin{pmatrix} \kappa_{11} & \kappa_{12} & \kappa_{13} \\ \kappa_{12} & \kappa_{22} & \kappa_{23} \\ \kappa_{13} & \kappa_{23} & \kappa_{33}, \end{pmatrix} \tag{21}$$

with

$$\begin{aligned}
\kappa_{11} &= m^2\left[\mathcal{A}^I_{\mathrm{e}\theta r\theta r} - \frac{p^2}{\mathcal{A}^I_{\mathrm{e}r\theta r\theta}}\right] + \mathcal{A}^I_{\mathrm{e}\theta\theta\theta\theta} + 2p + k_z^2 r^2\left(\mathcal{A}^I_{\mathrm{e}zrzr} - \frac{p^2}{\mathcal{A}^I_{\mathrm{e}rzrz}}\right) + \mathcal{A}^I_{\mathrm{e}rrrr},\\
\kappa_{12} &= m\left(\mathcal{A}^I_{\mathrm{e}\theta r\theta r} + \mathcal{A}^I_{\mathrm{e}\theta\theta\theta\theta} + 2p - \frac{p^2}{\mathcal{A}^I_{\mathrm{e}r\theta r\theta}} + \mathcal{A}^I_{\mathrm{e}rrrr}\right),\\
\kappa_{13} &= k_z r\left(\mathcal{A}^I_{\mathrm{e}rrrr} + p\right),\\
\kappa_{22} &= m^2\left(\mathcal{A}^I_{\mathrm{e}\theta\theta\theta\theta} + 2p + \mathcal{A}^I_{\mathrm{e}rrrr}\right) + \mathcal{A}^I_{\mathrm{e}\theta r\theta r} + k_z^2 r^2 \mathcal{A}^I_{\mathrm{e}z\theta z\theta} - \frac{p^2}{\mathcal{A}^I_{\mathrm{e}r\theta r\theta}},\\
\kappa_{23} &= k_z r m\left(2p + \mathcal{A}^I_{\mathrm{e}rrrr}\right),\\
\kappa_{33} &= m^2\mathcal{A}_{\mathrm{e}\theta z\theta z} + k_z^2 r^2\left(\mathcal{A}^I_{\mathrm{e}zzzz} + 2p + \mathcal{A}^I_{\mathrm{e}rrrr}\right).
\end{aligned} \tag{22}$$

In order to numerically solve the incremental equations in Eq.(19), we adopt the *surface impedance matrix method* to implement a robust numerical procedure. With the linear functional relation $r\mathbf{S} = \mathbf{ZU}$ (Destrade et al., 2009), we derive the following Riccati differential equation

$$\frac{\mathrm{d}\mathbf{Z}}{\mathrm{d}r} = \frac{1}{r}\left(\mathbf{G}_3 - \mathbf{Z}\mathbf{G}_1 - \mathbf{G}_1^T\mathbf{Z} - \mathbf{Z}\mathbf{G}_2\mathbf{Z}\right), \tag{23}$$

where $\mathbf{Z}$ is the *surface impedance matrix*.

To find the numerical solutions, we must perform numerical integration from the initial condition $\mathbf{Z}^o(r_o) = \mathbf{0}$ to the target condition $\det \mathbf{Z}^i(r_i) = 0$. The continuity condition $\mathbf{Z}^o(r_s) = \mathbf{Z}^i(r_s)$ is also employed to integrate numerically, since the radial stress, shear stress, and displacements are continuous at the interface between two layers. The initial condition and the target condition correspond to the traction-free boundary condition at the outer and inner surface, respectively.

3.2. Theoretical results of the linear stability analysis

Based on the linear stability analysis, we specifically investigate how geometrical incompatibility governs the onset of instability and pattern selection with varying stiffness ratio μ^o/μ^i and thickness ratio H^i/H^o of the layers. Fig.5 illustrates the influence of the geometrical incompatibility parameter interplaying with the stiffness ratio and the thickness ratio on the critical differential growth ratio and critical instability modes with 3D diagrams.

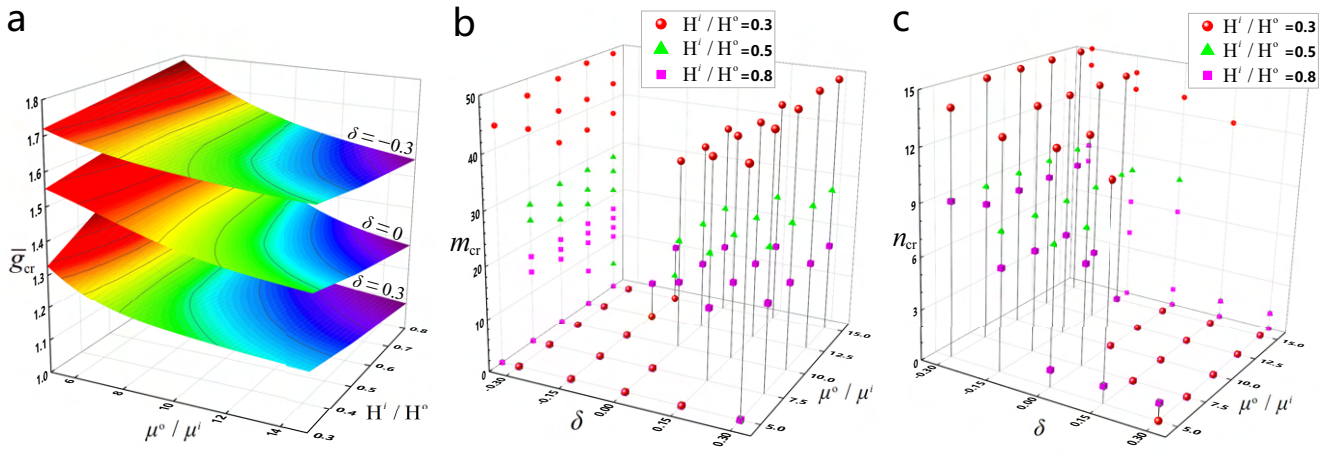

Figure 5: Critical differential growth ratio $\bar{g}_{cr}$(a) and the corresponding critical circumferential wavenumbers m_{cr}(b), and critical axial wavenumbers n_{cr}(c) for varying the geometrical incompatibility parameter δ, stiffness ratio μ^o/μ^i, and thickness ratio H^i/H^o of the bilayer tube at fixed $B/C = 0.75$. The marks on the vertical face are obtained by projection.

We first investigate the influence of geometrical incompatibility on the onset of buckling instability with varying stiffness ratio μ^o/μ^i and thickness ratio H^i/H^o (Fig.5(a)). As the stiffness ratio μ^o/μ^i of the layers increases, the critical differential growth ratio $\bar{g}_{cr}$ decreases. Besides, an increase in the thickness ratio H^i/H^o corresponds to a decreasing critical differential growth ratio when the stiffness ratio μ^o/μ^i is large ($\mu^o/\mu^i > 12.5$), but leads to a increasing critical differential growth ratio for a small stiffness ratio ($\mu^o/\mu^i < 7.5$). Notably, geometrical incompatibility always exerts a remarkable influence on the critical differential growth ratio $\bar{g}$, for any given stiffness ratio μ^o/μ^i and thickness ratio H^i/H^o. A positive geometrical incompatibility parameter ($\delta > 0$) leads to a decrease of the instability threshold, while a negative geometrical incompatibility parameter ($\delta < 0$) increases the instability threshold.

On the other hand, our linear stability analysis demonstrates that geometrical incompatibility also plays an improtant role in pattern selection. Fig.5(b) and Fig.5(c) give the critical circumferential wavenumber m_{cr} and the critical longitudinal wavenumber n_{cr} , respectively. An increase of the geometrical incompatibility parameter δ leads to an increasing critical circumferential wavenumber m_{cr} and a decreasing critical longitudinal wavenumber n_{cr}. Besides, it is found that the critical stiffness ratios for both circumferential instability and longitudinal instability decrease as the geometrical incompatibility parameter increases.

From Fig.5(b) and (c), we can conclude that the thinner the inner layer, the more wrinkles are generated. Nevertheless, the thickness ratio can govern pattern selection only in some specific cases, resulting in lack of generality. By contrast, the stiffness ratio can efficiently regulate pattern selection but has a slight effect on the wavenumbers of either circumferential or longitudinal patterns unfortunately. It is worth noting that geometrical incompatibility can not only guide pattern selection but also exerts a noticeable impact on the wavenumbers.

4. Experimental and numercial implementation

4.1. Experiments

We conduct experiments to explore the patterns formation and subsequent non-linear evolutions of the initial geometrically incompatible bilayer tubes induced by differential swelling. An initial geometrically incompatible bilayer tube consists of an inner hydrogel tube and an outer rubber tube. The inner hydrogel tube swells observably when immersed in water whereas the swelling of the rubber tube is negligible in the same environment. Particularly, hydrogel is deemed as a highly suitable material to mimic the growth of soft biological tissues.

In the experiments, the Mold Max$^{\text{TM}}$ 30 and Mold Star$^{\text{TM}}$ 15 SLOW are adopted to fabricate the rubber tubes, whose elastic moduli (color) are 759 kPa (pink) and 380 kPa (green), respectively. The manufacturing processes are following the instructions provided by the manufacturer. All rubber tubes have the same geometric parameters, with $B = 30$ mm, $C = 40$ mm, and $L = 70$ mm. To fabricate the hydrogel tubes, we prepare tubular acrylic molds that allow the penetration of ultraviolet ray. Then, the hydrogel tubes are fabricated following the fabrication process of (Han et al., 2020). The required elastic moduli for the hydrogel tubes can be obtained by changing the concentration of the monomer solution. For the sake of distinction, the yellow (green) color is selected for the inner hydrogel tube when the outer rubber tube is pink (green). Using the acrylic molds, we fabricate the hydrogel tubes with various sizes and thicknesses but have a uniform length of $L = 70$ mm.

Initially, the hydrogel tube and the rubber tube are radially incompatible but have the same length. We radially expand or compress the hydrogel tube to make it fully fits inside the rubber tube, and then glue the contact surface to obtain the perfectly bonded bilayer tube. To avoid dehydration of the hydrogel tube, the bilayer tube is placed in a constant humidity cabinet during the whole curing time of the glue. The length of both tubes are fixed and the bilayer tube is allowed to relax radially. Then, the bilayer tube is placed in an Acrylic frame whose headroom is identical to the length of bilayer tubes. Furthermore, the top and bottom plates of the Acrylic frame are fixed to confine the axial deformation. To make sure water can flow freely into the bilayer tubes during the whole swelling period, two circular holes are reserved both on the top and bottom plates on the axis of the bilayer tubes. The whole experimental setup is shown in Fig.6. Finally, we immerse the experimental setup into a water tank to observe the morphological evolution of the bilayer tubes induced by differential swelling. Images are taken every one hour for future analysis.

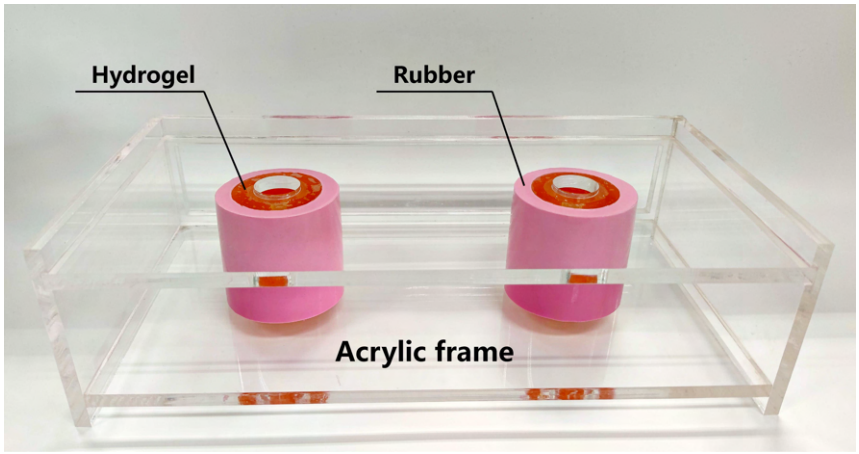

Figure 6: Experimental setup for exploiting geometrical incompatibility for guiding pattern selection in growing bilayer tubes.

4.2. Finite element simulations

In order to investigate pattern selection and the post-buckling behavior of initial geometrically incompatible bilayer cylindrical tubes in response to differential growth, the non-linear FE simulations are performed using the commercial software Abaqus (Version 6.13). We discretize both layers of the geometrically incompatible bilayer tube using eight-node hexahedral hybrid elements (C3D8H). An inherent interference fit methodology is adopted to implement the interference fit assembly of the geometrically incompatible bilayer tube. The distributions of residual stresses after interference fit remarkably agree with the theoretical analyses, as depicted in Fig.3. Thereafter, a thermal dilatation process are performed to model volumetric growth using a pseudo-dynamic method. To trigger the buckling instability, an initial geometrical imperfection is introduced from the eigenvalue buckling analysis. In this way, the FE simulation can well capture the patterns formation and subsequent morphological evolutions, as presented in the following section.

5. Results and discussions

In this section, we simultaneously present the results of theoretical analysis, numerical simulation, and swelling experiment. Our findings demonstrate that geometrical incompatibility can guide pattern selection and affect the post-buckling evolution of the emerging pattern. Furthermore, geometrical incompatibility can also guide pattern selection by coupling with the thickness ratio and the stiffness ratio. Both the results of FE simulation and swelling experiment are compared to our theoretical predictions, as shown below.

5.1. Pattern selection guided by geometrical incompatibility

Fig.7 illustrates the effect of geometrical incompatibility on the instability threshold and pattern selection of the growing bilayer tube. Based on the linear stability analysis, we separate Fig.7 into three distinct regions to denote three typical surface instability patterns. The left and right regions represent the longitudinal and circumferential patterns, respectively. The region between the longitudinal pattern and the circumferential pattern is characterized by the 2D pattern, in which the circumferential wrinkles and the longitudinal wrinkles emerge simultaneously. For the sake of presentation clarity, only half the length of the bilayer tubes in FE simulation are presented in this figure.

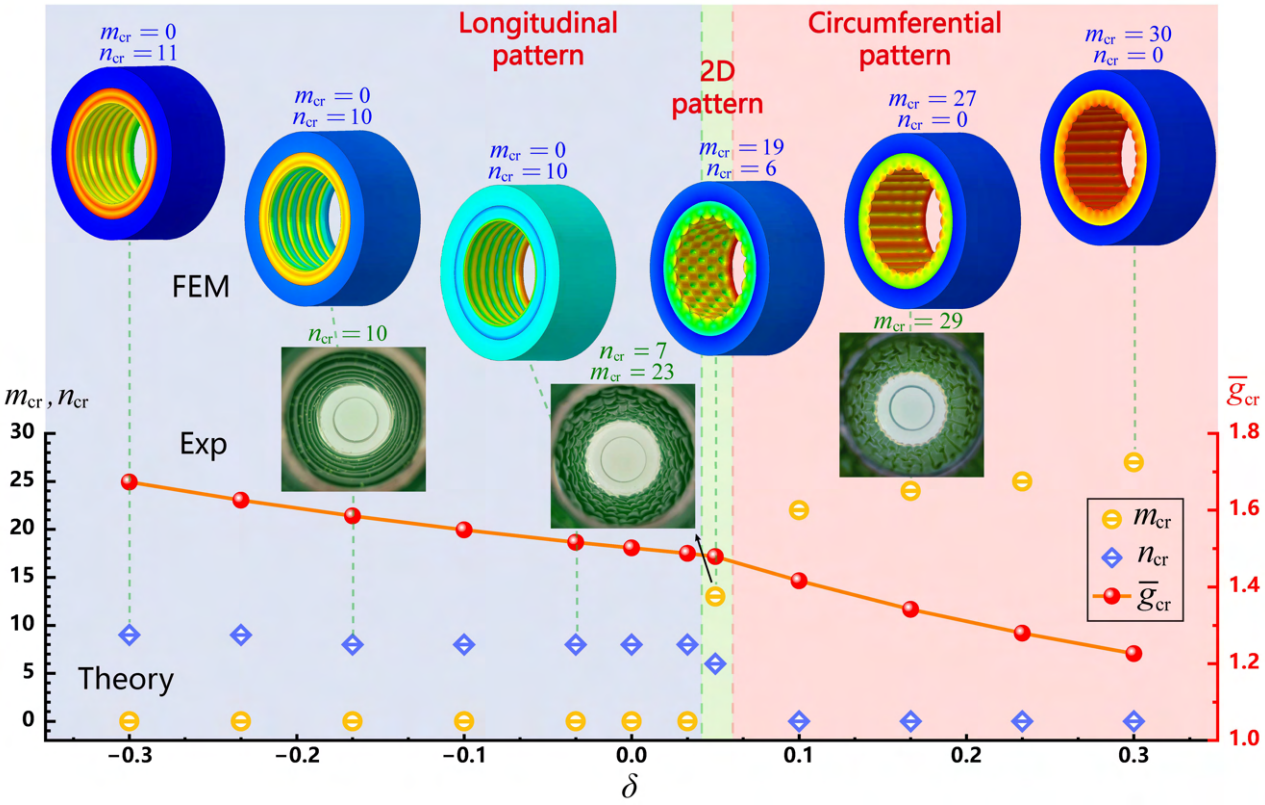

Figure 7: Influence of the geometrical incompatibility parameter δ on the instability threshold and pattern selection of the growing bilayer tubes with theoretical prediction, finite element (FE) simulation, and experimental observation. The parameters are set as $\mu^o/\mu^i = 7.5$, $H^i/H^o = 0.5$, and $B/C = 0.75$.

Fig.7 highlights that geometrical incompatibility has a significant influence on the instability threshold and pattern formation of the growing bilayer tube. In agreement with our theoretical prediction, both FE simulation and experiment show that all of the circumferential, longitudinal and 2D patterns can be captured at the inner surface by varying the geometrical incompatibility parameter. In particular, with the increase of the geometrical incompatibility parameter δ, the instability pattern transforms from the longitudinal pattern to the 2D pattern and then to the circumferential pattern. An increasing geometric incompatibility parameter δ also leads to a decrease of instability threshold $\bar{g}_{cr}$. Moreover, an increase of the geometrical incompatibility parameter ($\delta > 0.062$) tends to increase the wavenumber of the circumferential pattern m_{cr}. The wavenumber of the longitudinal pattern n_{cr} increases slowly as the geometrical incompatibility parameter decreases ($\delta < 0.042$). Notably, the results of FE simulation show the same trend of the critical wavenumbers varying with the geometrical incompatibility parameter. The wavenumbers of longitudinal instability pattern and circumferential instability pattern in our experiment also show good agreements with the theoretical predictions.

Fig.7 has shown how to guide pattern selection by adjusting the geometrical incompatibility parameter, for given stiffness ratio and thickness ratio. However, the stiffness ratio and thickness ratio have been demonstrated that they also affect pattern selection of growing bilayer tubes. In what follows, we will show how geometrical incompatibility guides pattern selection by coupling with the thickness ratio and the stiffness ratio. In addition, corresponding FE simulations and swelling experiments are performed to validate our theoretical model.

Phase diagrams spanned by μ^o/μ^i and δ, indicating the influence of geometrical incompatibility

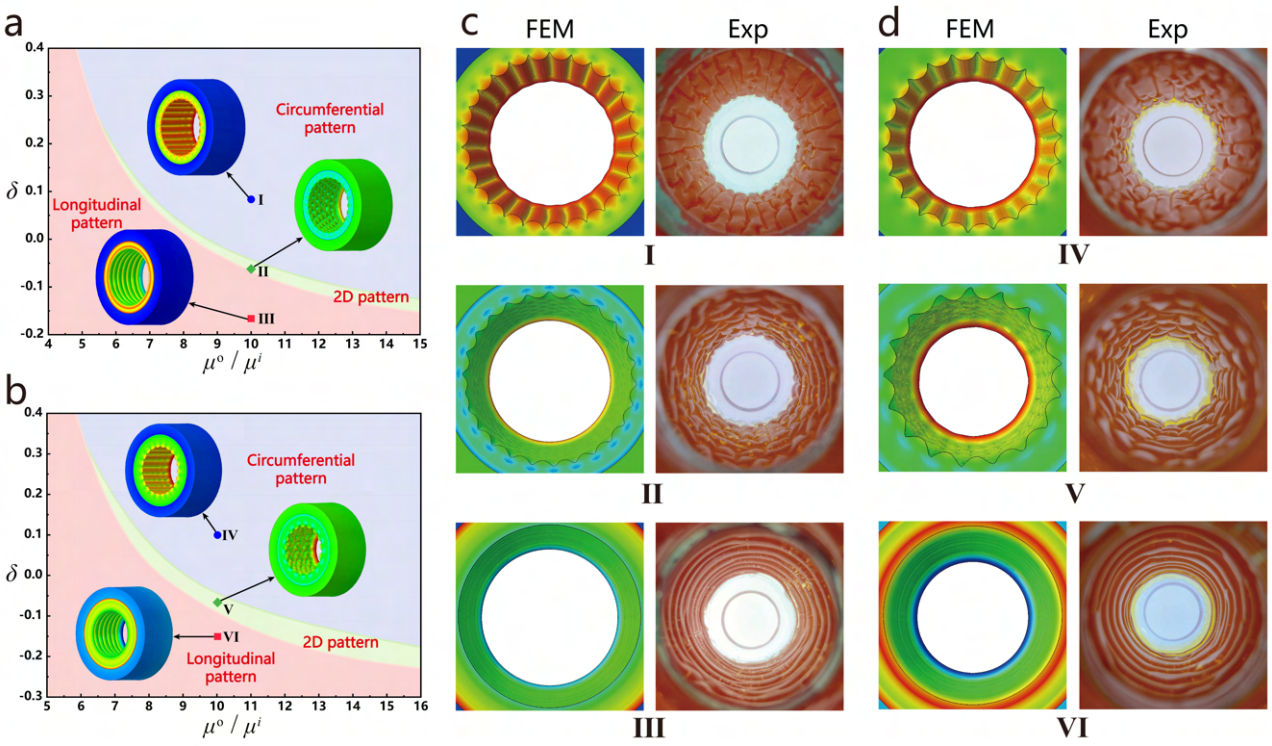

Figure 8: Linear stability analysis, FE simulation, and corresponding swelling experiment on pattern selection of the bilayer tubes. (a-b) Phase diagrams in the $(\mu^o/\mu^i, \delta)$-space with corresponding FE simulations, show the effect of geometrical incompatibility coupling with the stiffness ratio on pattern selection. The thickness ratio in two phase diagrams are $H^i/H^o = 0.5$(a) and $H^i/H^o = 0.8$(b), with fixed $B/C = 0.75$. (c-d) Top view results of FE simulations and swelling experiments, correspond to the markers in the three regions of (a) and (b).

on pattern selection with varying stiffness ratio, are depicted in Fig.8(a) and (b). In general, increasing either the geometrical incompatibility parameter or the stiffness ratio can provoke the instability pattern to transform from the longitudinal pattern to the 2D pattern and then to the circumferential pattern. However, the 2D pattern disappears when the geometrical incompatibility parameter is large than a critical value ($\delta > 0.34$) or the stiffness ratio is small than a critical value ($\mu^o/\mu^i < 5.4$). In addition, it is found that the critical geometrical incompatibility parameters for both circumferential and longitudinal instability patterns decrease as the stiffness ratio increases. Fig.8(c) and (d) display the results of numerical simulations and swelling experiments in the top view. In agreement with the phase diagrams predicted by linear stability analysis, the instability pattern undergoes a transtion from a circumferential pattern to a 2D pattern and than to a longitudinal pattern as the geometrical incompatibility parameter decrease. It worthy noting that the numbers of wrinkls in numerical simulations and swelling experiments are very close. Furthermore, the thinner inner layer of a bilayer tube (Fig.8(c)) generates more wrinkles than the thicker one (Fig.8(d)), which is consistent with the prediction of linear stability analysis in Fig.5.

Fig.9(a) and (b) give morphological phase diagrams for patterns selection in the $(H^i/H^o, \delta)$-spaces, which show how geometrical incompatibility governs pattern selection by coupling with the thickness ratio. Consistently, an increase of the geometrical incompatibility parameter leads to a morphological transition from a longitudinal pattern to a 2D pattern and then to a circumferential pattern. As depicted in Fig.9(a) and (b), an increasing inner layer thickness tends to expand the 2D pattern region. In particular, the 2D pattern is difficult to be captured on the thin

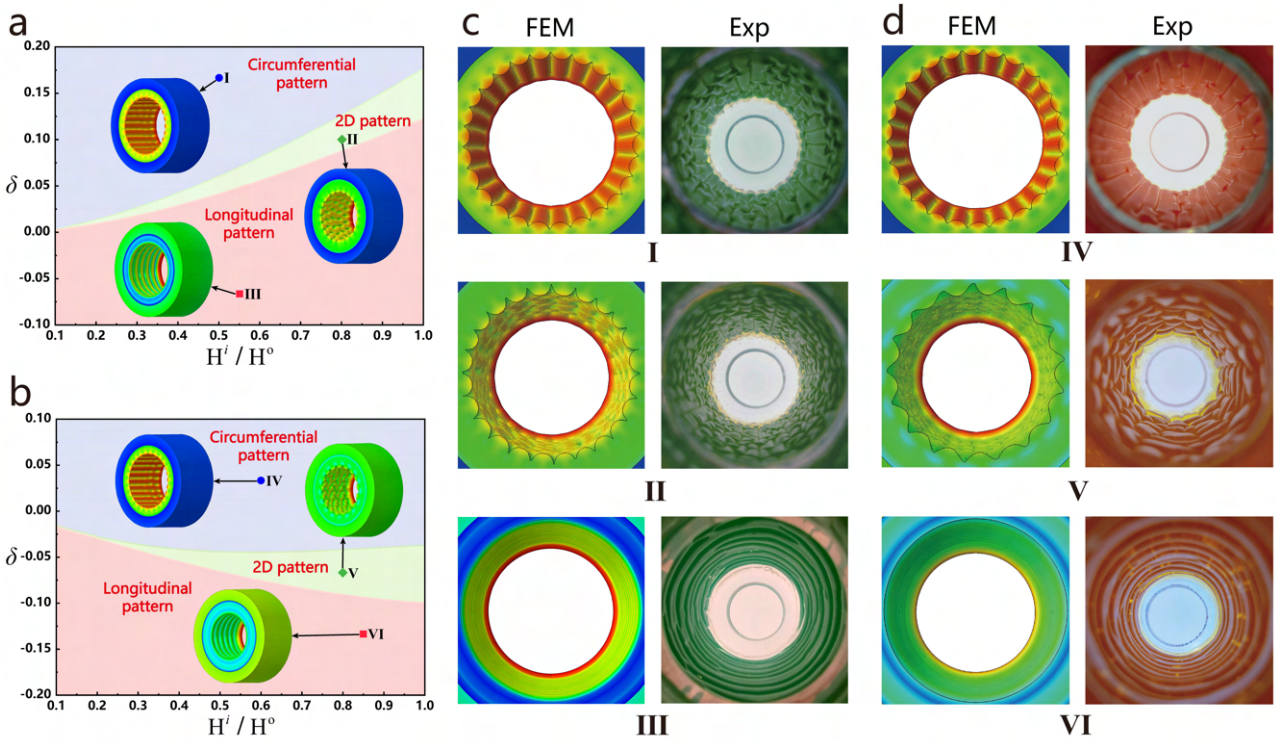

Figure 9: Linear stability analysis, FE simulation, and corresponding swelling experiment on pattern selection of the bilayer tubes. (a-b) Phase diagrams in the $(H^i/H^o, \delta)$-space with corresponding FE simulations, show the effect of geometrical incompatibility coupling with the thickness ratio on pattern selection. Stiffness ratio in two phase diagrams are $\mu^o/\mu^i = 7.5$(a) and $\mu^o/\mu^i = 10$(b), with fixed $B/C = 0.75$. (c-d) Top view results of FE simulations and swelling experiments, correspond to the markers in the three regions of (a) and (b).

inner layer ($H^i/H^o < 0.18$). Moreover, by comparing Fig.9(a) and Fig.9(b), it can be inferred that the stiffness ratio determines how the thickness ratio affects pattern selection of the growing bilayer tube. Similarly, the phase diagrams predicted by linear stability analysis are verified both numerically and experimentally, as illustrated in Fig.9(c) and (d).

5.2. Post-buckling evolutions

Understanding the post-buckling evolution of a growing bilayer tubular soft matter is also of great significance for disease diagnosis and 4D printing. In this subsection, we numerically and experimentally investigate the effect of geometrical incompatibility on pattern formation, as well as the post-buckling evolution of the emerging pattern in the fully non-linear regime. In the following, we will show the post-buckling evolutions of circumferential, longitudinal and 2D patterns primarily prescribed by geometrical incompatibility.

Formation and evolution of circumferential pattern: Fig.10 illustrates the circumferential pattern formation and the post-buckling evolution of the emerging instability pattern. Fig.10(a) and (e) show that the inner surface of the bilayer tube is smooth before growth/swelling. With the gradual accumulation of circumferential compressive stress that arisen from differential growth/swelling, critical circumferential instability occurs at the inner surface, as shown in Fig.10(b) and (f). As differential growth/swelling continues, the amplitude of the circumferential pattern increases but the wavenumber remains unchanged, as depicted in Fig.10(c-d) and (g-h). Note that the slight decrease of the wrinkles in the swelling experiment is mainly due to the initial transient instability induced by the inhomogeneous swelling of the hydrogel tube (Ilseng et al., 2019; Curatolo et al.,

2017). In other words, the instability pattern induced by homogeneous swelling is the desired result corresponding to our theoretical model.

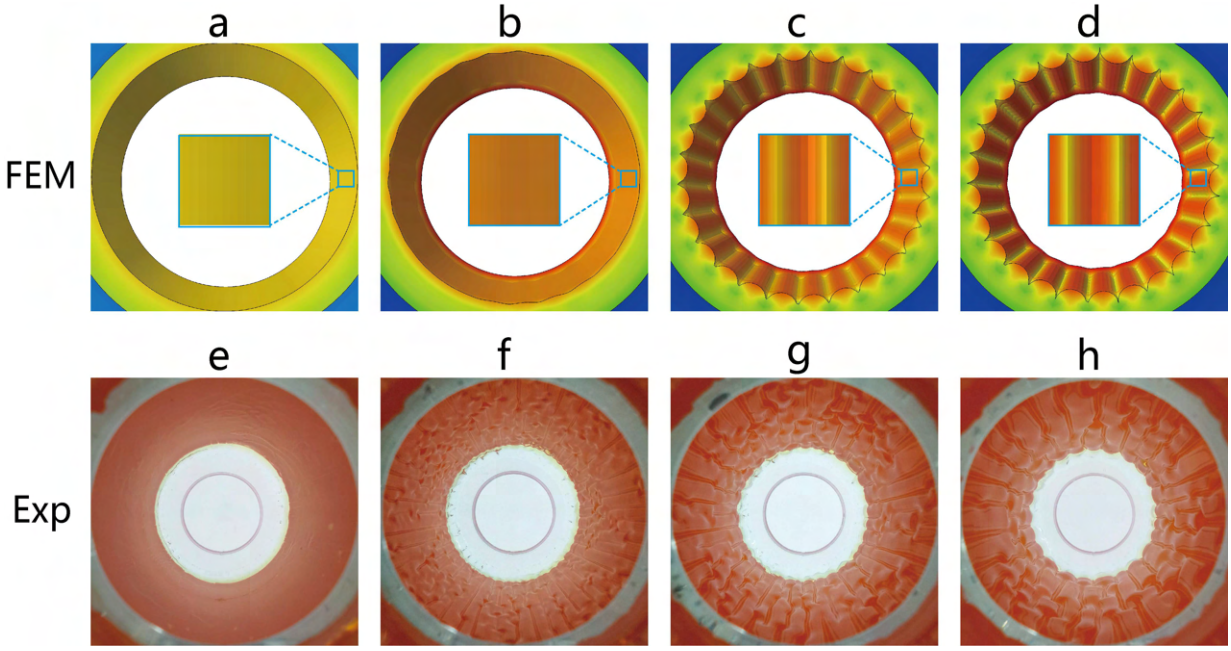

Figure 10: Comparison of the formation and subsequent morphological evolution of the circumferential instability pattern between FE simulation (a-d) and experimental observation (e-h); (a) and (e) show the initial state before growth/swelling; (b-d) and (f-h) depict the onset of buckling instability and the post-buckling evolution of the growing bilayer tube. The parameters are set as $\delta = 1/6$, $\mu^o/\mu^i = 10$, $H^i/H^o = 0.5$, and $B/C = 0.75$.

Formation and evolution of longitudinal pattern: Fig.11 shows the longitudinal pattern formation, as well as the morphological evolution of longitudinal pattern in the post-buckling regime. A negative geometrical incompatibility parameter prescribes a tensile residual stress field within the inner layer (Fig.11(a) and (e)). Then, the axial compressive stress is generated in response to gradually differential growth/swelling and then leads to longitudinal instability of the inner layer, as shown in Fig.11(b) and (f). With the continuous growth/swelling of the inner layer, the wrinkles become increasing deeper whereas the wavenumber is constant, as seen in Fig.11(c-d). Similar to the post-buckling evolution of circumferential pattern, the wrinkles in our swelling experiment undergo a slight decrease, as depicted in Fig.11(g-h). As expected, Fig.11(h) is in good agreement with the result of FE simulation (Fig.11(d)).

Formation and evolution of 2D pattern: In Fig.12, the 2D pattern formation in a bilayer tube induced by differential growth/swelling, as well as the post-buckling evolution of the 2D pattern are demonstrated. Fig.12(a) and (e) give a stress free bilayer tube with a smooth inner surface. As seen in Fig.12(b) and (f), the inner surface of a growing bilayer tube is characterized by a 2D instability pattern when the circumferential and axial compressive stresses reach the critical value almost simultaneously. Then, with further growth/swelling of the inner layer, the 2D pattern deepens gradually and a secondary bifurcation is observed when the amplitude of the 2D pattern reaches a critical value. The nearby circular shapes interact with each other and then the symmetry of the pattern is abruptly broken, leading to a transition from a dimple into a herringbone pattern (Fig.12(c-d)). Furthermore, a secondary bifurcation is also observed in our swelling experiment as shown in Fig.12(g-h).

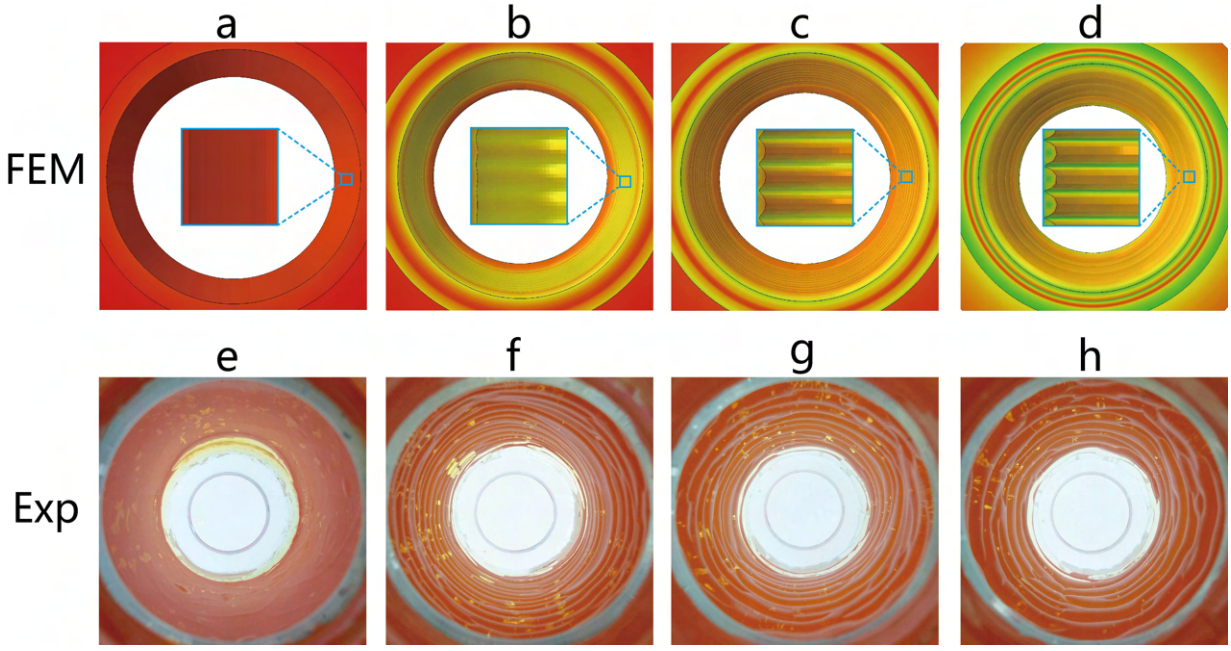

Figure 11: Comparison of the formation and subsequent morphological evolution of the longitudinal instability pattern between FE simulation (a-d) and experimental observation (e-h); (a) and (e) show the initial state before growth/swelling, (b-d) and (f-h) depict the onset of buckling instability and the post-buckling evolution of the growing bilayer tube. The parameters are set as $\delta = -1/6$, $\mu^o/\mu^i = 10$, $H^i/H^o = 0.5$, and $B/C = 0.75$.

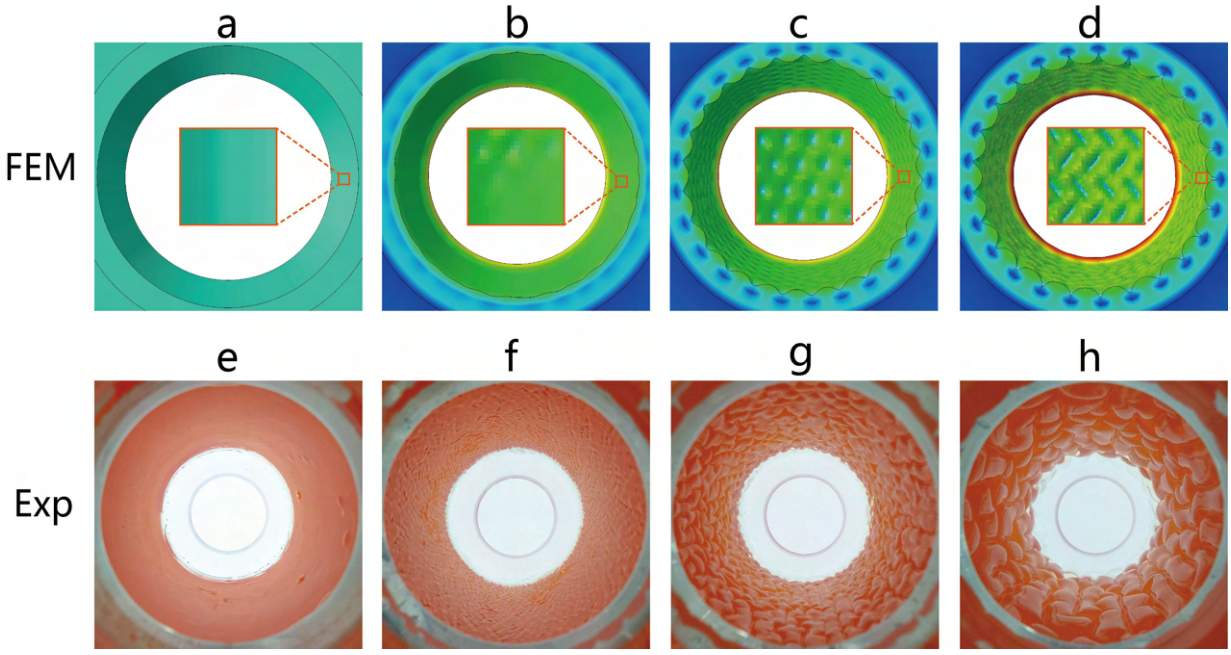

Figure 12: Comparison of the formation and subsequent morphological evolution of the 2D instability pattern between FE simulation (a-d) and experimental observation (e-h); (a) and (e) show the initial state before growth/swelling, (b-d) and (f-h) depict the onset of buckling instability and the post-buckling evolution of the growing bilayer tube. The parameters are set as $\delta = 0$, $\mu^o/\mu^i = 8.5$, $H^i/H^o = 0.5$, and $B/C = 0.75$.

6. Conclusions

In summary, we have established an improved theoretical model and implemented a series of quantificational experiments and numerical simulations to investigate how geometrical incompatibility governs pattern selection and subsequent morphological evolutions in growing bilayer tubes. The results demonstrate that geometrical incompatibility indeed plays an important role in pattern selection, as well as the post-buckling evolution of the emerging patterns. As the geometrical incompatibility parameter increases, the instability pattern undergoes a transition from a longitudinal pattern to a 2D pattern and then to a circumferential pattern. Furthermore, we find that geometrical incompatibility can also guide pattern selection by coupling with the thickness ratio and stiffness ratio of the bilayer tubes. Phase diagrams on pattern selection are derived from theoretical computations and have been validated numerically and experimentally. Notably, both the numerical simulations and experimental observations are consistent with our theoretical predictions. A secondary bifurcation has been observed in the post-buckling evolution of the 2D pattern with continuous growth far beyond the critical state. Our findings provide, both experimentally and theoretically, a fundamental understanding of surface pattern formation in growing biological tissues. In addition, geometrical incompatibility can also be exploited for guiding pattern selection of other geometric configurations, such as core-shell spheres and composite plates.

Acknowledgments

This work was supported by the National Natural Science Foundation of China through grants No.11925206 and No.11772295.

References

Hillel Aharoni, Desislava V. Todorova, Octavio Albarrán, Lucas Goehring, Randall D. Kamien, and Eleni Katifori. The smectic order of wrinkles. *Nat Commun*, 8(1):15809, 2017.

Hyung Jong Bae, Sangwook Bae, Jinsik Yoon, Cheolheon Park, Kibeom Kim, Sunghoon Kwon, and Wook Park. Self-organization of maze-like structures via guided wrinkling. *Sci. Adv.*, 3(6): e1700071, 2017.

V. Balbi, E. Kuhl, and P. Ciarletta. Morphoelastic control of gastro-intestinal organogenesis: Theoretical predictions and numerical insights. *J. Mech. Phys. Solids*, 78:493–510, 2015.

Wilson Barros, Eduardo N. de Azevedo, and Mario Engelsberg. Surface pattern formation in a swelling gel. *Soft Matter*, 8(32):8511, 2012.

M. Ben Amar and F. Jia. Anisotropic growth shapes intestinal tissues during embryogenesis. *Proc Natl Acad Sci USA*, 110(26):10525–10530, 2013.

M. Ben Amar, C. Chatelain, and P. Ciarletta. Contour Instabilities in Early Tumor Growth Models. *Phys. Rev. Lett*, 106(14):148101, 2011.

Martine Ben Amar and Alain Goriely. Growth and instability in elastic tissues. *J. Mech. Phys. Solids*, 53(10):2284–2319, 2005.

Adrian Buganza Tepole, Michael Gart, Chad A Purnell, Arun K Gosain, and Ellen Kuhl. The incompatibility of living systems: characterizing growth-induced incompatibilities in expanded skin. *Ann.Biomed.Eng*, 44(5):1734–1752, 2016.

Noè Caruso, Aleksandar Cvetković, Alessandro Lucantonio, Giovanni Noselli, and Antonio DeSimone. Spontaneous morphing of equibiaxially pre-stretched elastic bilayers: the role of sample geometry. *Int. J. Mech. Sci*, 149:481–486, 2018.

Aditi Chakrabarti, Thomas C. T. Michaels, Sifan Yin, Eric Sun, and L. Mahadevan. The cusp of an apple. *Nat. Phys*, 17(10):1125–1129, 2021.

Nontawit Cheewaruangroj and John S. Biggins. Pattern selection when a layer buckles on a soft substrate. *Soft Matter*, 15(18):3751–3770, 2019.

P. Ciarletta. Buckling Instability in Growing Tumor Spheroids. *Phys. Rev. Lett.*, 110(15):158102, 2013.

P. Ciarletta, V. Balbi, and E. Kuhl. Pattern Selection in Growing Tubular Tissues. *Phys. Rev. Lett*, 113(24):248101, 2014.

P. Ciarletta, M. Destrade, A.L. Gower, and M. Taffetani. Morphology of residually stressed tubular tissues: Beyond the elastic multiplicative decomposition. *J. Mech. Phys. Solids*, 90:242–253, 2016.

Michele Curatolo, Paola Nardinocchi, Eric Puntel, and Luciano Teresi. Transient instabilities in the swelling dynamics of a hydrogel sphere. *Journal of Applied Physics*, 122(14):145109, 2017.

Benny Davidovitch, Yiwei Sun, and Gregory M. Grason. Geometrically incompatible confinement of solids. *Proc Natl Acad Sci USA*, 116(5):1483–1488, January 2019.

Julien Dervaux and Martine Ben Amar. Morphogenesis of Growing Soft Tissues. *Phys. Rev. Lett*, 101(6):068101, 2008.

Julien Dervaux and Martine Ben Amar. Buckling condensation in constrained growth. *J. Mech. Phys. Solids*, 59(3):538–560, 2011.

Julien Dervaux, Yves Couder, Marie-Alice Guedeau-Boudeville, and Martine Ben Amar. Shape Transition in Artificial Tumors: From Smooth Buckles to Singular Creases. *Phys. Rev. Lett.*, 107(1):018103, 2011.

Michel Destrade, Aisling Ní Annaidh, and Ciprian D. Coman. Bending instabilities of soft biological tissues. *Int. J. Solids. Struct*, 46(25):4322–4330, 2009.

Yanling Dou, Yanhua Fan, Jingbo Zhao, and Hans Gregersen. Longitudinal residual strain and stress-strain relationship in rat small intestine. *BioMed Eng OnLine*, page 37, 2006.

Yangkun Du, Chaofeng Lü, Weiqiu Chen, and Michel Destrade. Modified multiplicative decomposition model for tissue growth: Beyond the initial stress-free state. *J. Mech. Phys. Solids*, 118: 133–151, 2018.

Yangkun Du, Chaofeng Lü, Michel Destrade, and Weiqiu Chen. Influence of Initial Residual Stress on Growth and Pattern Creation for a Layered Aorta. *Sci. Rep*, 9(1):8232, 2019a.

Yangkun Du, Chaofeng Lü, Congshan Liu, Zilong Han, Jian Li, Weiqiu Chen, Shaoxing Qu, and Michel Destrade. Prescribing patterns in growing tubular soft matter by initial residual stress. *Soft Matter*, 15(42):8468–8474, 2019b.

Yangkun Du, Yipin Su, Chaofeng Lü, Weiqiu Chen, and Michel Destrade. Electro-mechanically guided growth and patterns. *Journal of the Mechanics and Physics of Solids*, 143:104073, 2020.

Randall M. Erb, Jonathan S. Sander, Roman Grisch, and André R. Studart. Self-shaping composites with programmable bioinspired microstructures. *Nat Commun*, 4(1):1712, 2013.

Qi Ge, H. Jerry Qi, and Martin L. Dunn. Active materials by four-dimension printing. *Appl. Phys. Lett.*, 103(13):131901, 2013.

N Gjorevski, M Nikolaev, TE Brown, O Mitrofanova, N Brandenberg, FW DelRio, FM Yavitt, P Liberali, KS Anseth, and MP Lutolf. Tissue geometry drives deterministic organoid patterning. *Science*, 375:eaaw9021, 2022.

Alain Goriely. *The Mathematics and Mechanics of Biological Growth*, volume 45 of *Interdisciplinary Applied Mathematics*. Springer, New York, NY, 2017.

Alain Goriely and Martine Ben Amar. Differential Growth and Instability in Elastic Shells. *Phys. Rev. Lett*, 94(19):198103, 2005.

A. L. Gower, P. Ciarletta, and M. Destrade. Initial stress symmetry and its applications in elasticity. *Proc. R. Soc. A.*, 471(2183):20150448, 2015.

Zilong Han, Peng Wang, Guoyong Mao, Tenghao Yin, Danming Zhong, Burebi Yiming, Xiaocheng Hu, Zheng Jia, Guodong Nian, Shaoxing Qu, et al. Dual ph-responsive hydrogel actuator for lipophilic drug delivery. *ACS applied materials & interfaces*, 12(10):12010–12017, 2020.

Gerhard A. Holzapfel, Gerhard Sommer, Martin Auer, Peter Regitnig, and Ray W. Ogden. Layer-Specific 3D Residual Deformations of Human Aortas with Non-Atherosclerotic Intimal Thickening. *Ann Biomed Eng*, 35(4):530–545, 2007.

Changjin Huang, Zilu Wang, David Quinn, Subra Suresh, and K. Jimmy Hsia. Differential growth and shape formation in plant organs. *Proc Natl Acad Sci USA*, 115(49):12359–12364, 2018.

Arne Ilseng, Victorien Prot, Bjørn H. Skallerud, and Bjørn T. Stokke. Buckling initiation in layered hydrogels during transient swelling. *J. Mech. Phys. Solids*, 128:219–238, 2019.

Bo Li, Yan-Ping Cao, Xi-Qiao Feng, and Huajian Gao. Surface wrinkling of mucosa induced by volumetric growth: Theory, simulation and experiment. *J. Mech. Phys. Solids*, 59(4):758–774, 2011a.

Bo Li, Fei Jia, Yan-Ping Cao, Xi-Qiao Feng, and Huajian Gao. Surface Wrinkling Patterns on a Core-Shell Soft Sphere. *Phys. Rev. Lett*, 106(23):234301, 2011b.

Congshan Liu, Yangkun Du, Chaofeng Lü, and Weiqiu Chen. Growth and patterns of residually stressed core–shell soft sphere. *Int. J. Non-Linear Mech*, page 7, 2020.

Yin Liu, Xiaosong Yang, Yang Cao, Zhao Wang, Biaosong Chen, Jianjun Zhang, and Hongwu Zhang. Dehydration of core/shell fruits. *Computers & Graphics*, 47:68–77, 2015.

D.E. Moulton and A. Goriely. Circumferential buckling instability of a growing cylindrical tube. *J. Mech. Phys. Solids*, 59(3):525–537, 2011.

Alexandra B Rebocho, Paul Southam, J Richard Kennaway, J Andrew Bangham, and Enrico Coen. Generation of shape complexity through tissue conflict resolution. *eLife*, page 45, 2015.

Edward K. Rodriguez, Anne Hoger, and Andrew D. McCulloch. Stress-dependent finite growth in soft elastic tissues. *J. Biomech*, 27(4):455–467, 1994.

Thierry Savin, Natasza A. Kurpios, Amy E. Shyer, Patricia Florescu, Haiyi Liang, L. Mahadevan, and Clifford J. Tabin. On the growth and form of the gut. *Nature*, 476(7358):57–62, 2011.

M. Shams, M. Destrade, and R. W. Ogden. Initial stresses in elastic solids: Constitutive laws and acoustoelasticity. *Wave Motion*, 48(7):552–567, 2011.

A. E. Shyer, T. Tallinen, N. L. Nerurkar, Z. Wei, E. S. Gil, D. L. Kaplan, C. J. Tabin, and L. Mahadevan. Villification: How the Gut Gets Its Villi. *Science*, 342(6155):212–218, 2013.

Dimitrios P. Sokolis, Nausicaa Gouskou, Stavroula A. Papadodima, and Stavros K. Kourkoulis. Layer-Specific Residual Deformations and Their Variation Along the Human Aorta. *J. Biomech. Eng*, 143:094504, 2021.

Gerhard Sommer, Peter Regitnig, Lukas Költringer, and Gerhard A. Holzapfel. Biaxial mechanical properties of intact and layer-dissected human carotid arteries at physiological and supraphysiological loadings. *Am.J.Physiol*, 298(3):H898–H912, 2010.

Paul Steinmann. Geometrical foundations of continuum mechanics. *Lecture Notes in Applied Mathematics and Mechanics*, 2, 2015.

Triantafyllos Stylianopoulos, John D. Martin, Vikash P. Chauhan, Saloni R. Jain, Benjamin Diop-Frimpong, Nabeel Bardeesy, Barbara L. Smith, Cristina R. Ferrone, Francis J. Hornicek, Yves Boucher, Lance L. Munn, and Rakesh K. Jain. Causes, consequences, and remedies for growth-induced solid stress in murine and human tumors. *Proc. Natl. Acad. Sci. U.S.A.*, 109(38): 15101–15108, 2012.

A. Sydney Gladman, Elisabetta A. Matsumoto, Ralph G. Nuzzo, L. Mahadevan, and Jennifer A. Lewis. Biomimetic 4D printing. *Nat. Mater*, 15(4):413–418, 2016.

Héloïse Thérien-Aubin, Zi Liang Wu, Zhihong Nie, and Eugenia Kumacheva. Multiple Shape Transformations of Composite Hydrogel Sheets. *J. Am. Chem. Soc.*, 135(12):4834–4839, 2013.

Charles Melbern Wilcox, Miguel Muñoz-Navas, and Joseph Jy Sung. *Atlas of Clinical Gastrointestinal Endoscopy: Expert Consult-Online and Print*. Elsevier Health Sciences, 2012.

Hang Xiao and Xi Chen. Modeling and simulation of curled dry leaves. *Soft Matter*, 7(22):10794, 2011.

Fan Xu, Chenbo Fu, and Yifan Yang. Water Affects Morphogenesis of Growing Aquatic Plant Leaves. *Phys. Rev. Lett*, 124(3):038003, 2020a.

Fan Xu, Shichen Zhao, Conghua Lu, and Michel Potier-Ferry. Pattern selection in core-shell spheres. *J. Mech. Phys. Solids*, 137:103892, 2020b.

Jie Yin, Xi Chen, and Izhak Sheinman. Anisotropic buckling patterns in spheroidal film/substrate systems and their implications in some natural and biological systems. *J. Mech. Phys. Solids*, 57(9):1470–1484, 2009.

Jingbo Zhao, Xudong Chen, Jian Yang, Donghua Liao, and Hans Gregersen. Opening angle and residual strain in a three-layered model of pig oesophagus. *J. Biomech*, 40:3187–3192, 2007.